

Article

Catalytic Degradation of Tetracycline Hydrochloride by Coupled UV–Peroxydisulfate System: Efficiency, Stability and Mechanism

Panfeng Ma, Yu Shi, Jingsen Zhang, Weijia Zhang, Yong Cao and Bingtao Liu *

School of Environment and Municipal Engineering, North China University of Water Resources and Electric Power, Zhengzhou 450046, China; mapanfeng1010@163.com (P.M.); syu1207@163.com (Y.S.); zhangjingsen0825@163.com (J.Z.); zwj_yiyi1002@163.com (W.Z.); ncwucy@sina.com (Y.C.)

* Correspondence: liubingtao@ncwu.edu.cn

Abstract: Magnetic CuFe_2O_4 powder obtained by sol–gel method and coupled photocatalysis was used to activate peroxydisulfate for tetracycline (TC) removal. A scanning electron microscope, X–ray diffraction Raman spectroscopy and FT–TR were used to characterize the catalysts. The degradation efficiency and stability of TC were highest under neutral conditions. The TC degradation rate reached 91.1% within 90 min. The removal rate of total organic carbon reaches 39.6% under optimal conditions. The unique electron transfer property of CuFe_2O_4 was utilized to achieve the synergistic effect of photocatalysis and persulfate oxidation. The main oxidizing substances involved in the decomposition were sulfate radicals and hydroxyl radicals, and the removal rate of over 84% could be maintained after five cycles of experiments.

Keywords: advanced oxidation; CuFe_2O_4 ; photocatalytic; peroxydisulfate; tetracycline



Citation: Ma, P.; Shi, Y.; Zhang, J.; Zhang, W.; Cao, Y.; Liu, B. Catalytic Degradation of Tetracycline Hydrochloride by Coupled UV–Peroxydisulfate System: Efficiency, Stability and Mechanism. *Processes* **2023**, *11*, 1638. <https://doi.org/10.3390/pr11061638>

Academic Editors: Panyue Zhang, Zhen Wu and Yan Wu

Received: 9 April 2023

Revised: 22 May 2023

Accepted: 24 May 2023

Published: 26 May 2023



Copyright: © 2023 by the authors. Licensee MDPI, Basel, Switzerland. This article is an open access article distributed under the terms and conditions of the Creative Commons Attribution (CC BY) license (<https://creativecommons.org/licenses/by/4.0/>).

1. Introduction

As a kind of drug to prevent and treat bacterial diseases, antibiotics are used in a wide range of industries such as the medical industry, pharmaceutical industry and breeding industry [1]. Conventional wastewater treatment plants are unable to effectively treat antibiotics entering water bodies. Moreover, due to the long residence time of antibiotics and the low rate of microbial degradation in water, resulting in large amounts of antibiotic residues accumulating in natural water bodies [2]. This may increase the probability of the antibiotic resistance gene appearing, thus posing a threat to ecosystems. Tetracycline (TC) is widely used in veterinary medicine and aquaculture. The production and use of TC is the second largest antibiotic in global [3]. It plays a significant role in environmental protection and human health to explore an efficient and low–cost technology to remove TC from water bodies.

Advanced oxidation technology of sulfate radical ($\text{SO}_4^{\bullet-}$) has attracted widespread interest [4]. Persulfate advanced oxidation method has been shown to be a very effective strategy for antibiotic degradation [5,6]. The persulfate itself is a strong oxidant ($E_0 = 2.01$ V) [7]. The activation can generate $\text{SO}_4^{\bullet-}$ with higher potential. The rapid decomposition and final mineralization of organic matter can be achieved through $\text{SO}_4^{\bullet-}$. Compared with Fenton advanced oxidation technology which generates hydroxyl radical ($\bullet\text{OH}$), the advanced oxidation technology based on persulfate has the following characteristics: the redox potential of $\text{SO}_4^{\bullet-}$ standard ($E_0 = 2.5\text{--}3.1$ V) is higher than that of $\bullet\text{OH}$ ($E_0 = 1.9\text{--}2.7$ V). The oxidation principle is also similar to that of $\bullet\text{OH}$, but with a longer stabilization time. Additionally, it has a wider pH applicability range. Advanced oxidation of persulfate is more environmentally friendly than other degradation methods because it does not produce large amounts of waste material, nor does it consume a great deal of energy [8].

In recent years, CuFe_2O_4 magnetic materials have attracted great interest as an non-homogeneous catalyst applied to advanced oxidation process systems (AOPs). Li et al. [9] prepared $\text{Cu}/\text{CuFe}_2\text{O}_4$ composites using the solvothermal method. It was observed that both $\text{SO}_4^{\bullet-}$ and $\bullet\text{OH}$ are the main activation products, indicating that CuFe_2O_4 could activate persulfate. Xu et al. [10] have found that the peroxymonosulfate (PMS) can produce free radicals to remove bisphenol A in aqueous solutions with CuFe_2O_4 magnetic nanoparticles, and the removal rate of BPA reached 92.3% within 60 min. Furthermore, CuFe_2O_4 can be used as a photocatalyst. Jing et al. [11] studied the separate porous tetragonal- CuFe_2O_4 nanotubes coupled with photocatalytic degradation of acid fuchsin, indicating that CuFe_2O_4 has good photocatalytic activity and durability. The photocatalytic and persulfate oxidation system also has an abundance of highly reactive oxide species. Persulfate can generate $\text{SO}_4^{\bullet-}$ and $\bullet\text{OH}$ by capturing photo-generated electrons. Thus, using UV activated persulfate can achieve highly efficient removal of pollutants [12].

In this study, the combination of ultraviolet light (UV) and peroxodisulfate (PDS) was investigated for the removal of TC. The magnetically separable nano copper ferrite was prepared by sol-gel method and their structural features were characterized. The $\text{CuFe}_2\text{O}_4/\text{UV}/\text{PDS}$ system was constructed to degrade TC and the total organic carbon (TOC) was investigated. The effect of pH on the degradation performance and the reusability of CuFe_2O_4 were investigated. Additionally, the active species in the system were obtained by quenching experiments.

2. Materials and Methods

2.1. Chemicals

The water used in the experiment was deionized water. The other reagents were analytical reagents.

2.2. Synthesis of CuFe_2O_4

Magnetic nanometer copper ferrite was prepared by the sol-gel method [13]. Firstly, adding $\text{Cu}(\text{NO}_3)_2 \cdot 3\text{H}_2\text{O}$ (Shanghai Maclean Biochemical Technology Co., Shanghai, China), $\text{Fe}(\text{NO}_3)_3 \cdot 9\text{H}_2\text{O}$ (Tianjin Komio Chemical Reagent Co., Tianjin, China) and citric acid (Tianjin Fengchuan Sliding Chemical Reagent Technology Co., Tianjin, China) in the molar ratio of 1:2:3 to deionized water and stir well, and stirred until dissolved. The pH of the mixed solution was then adjusted to 7 with ammonia (Yantai Shuangshuang Chemical Co., Yantai, Shandong, China). Secondly, the solution was transferred to a water bath at 70 °C with continuous stirring until the water evaporated to form a dark green gel. The gel was dried for 7 h at 130 °C. Finally, the obtained dry gel was calcined at 200 °C, 300 °C, 400 °C, 500 °C and 600 °C for 2 h to afford the catalyst.

2.3. Analysis Methods

The scanning electron microscope (SEM, JSM-6700F, JEOL, Tokyo, Japan) was used to observe the microscopic morphology and structure of catalytic materials. The X-ray diffraction (XRD) patterns of CuFe_2O_4 was carried out on Dmax 2500 V Advance diffractometer (Bruker Co, Billerica, MA, USA) using $\text{Cu K}\alpha$ radiation ($\lambda = 0.15406$ nm) at a scanning rate of 5°/min with 2θ ranging between 10° and 80°. Raman spectrometer (HORIBA HR Evolution, HORIBA Co., Kyoto, Japan) with a laser wavelength of 532 nm was used in the range of 200–1200 cm^{-1} . The different functional groups and lattice vibrations of prepared systems were monitored by Fourier-transform infrared. (FT-IR, Is50FT-IR, American Thermal Power Company, Boston, MA, USA). The absorbance of TC solution was analyzed by UV-VIS spectrometer (N5000, Shanghai Youke Co., Shanghai, China) at a wavelength of 357 nm. To determine the removal rate of total organic carbon by TOC analyzer (Trace Elemental Instruments, XPERT, Delft, The Netherlands) was used. The pH_{zpc} of CuFe_2O_4 material was determined by intermittent equilibrium technique.

2.4. TC Degradation Experiments

The 0.02 g of CuFe_2O_4 was weighed into a beaker. Then, add 100 mL of TC solution with a concentration of 20 mg/L to the beaker. The solution was put into a dark box and stirred magnetically for 30 min. After that, 0.7 mM of PDS was added under continuous stirring and UV light (Royal Dutch Philips, $\lambda = 254$ nm) source was turned on. The light source is located above the beaker and the distance to the beaker is 15 cm. Samples were acquired when the reaction time was 0, 5, 10, 15, 30, 45 and 60 min, respectively. The TC solution concentration was determined by UV–VIS spectrometer after filtration with 0.45 μm filter membrane.

3. Results and Discussion

3.1. Characterization of CuFe_2O_4

The SEM analysis of CuFe_2O_4 calcined at 300 °C was carried out, and the results are shown in Figure 1. It is seen that the particles are on the nanometer scale. There are many particles on the surface of the material with uniform particle size dispersion, and these raised particles are CuFe_2O_4 crystals.

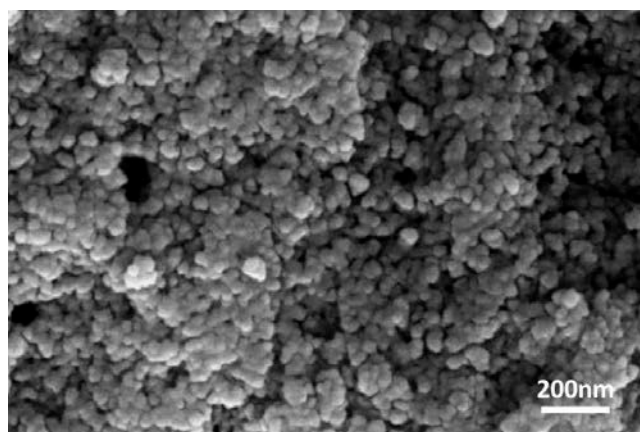


Figure 1. The SEM of CuFe_2O_4 .

Figure 2 shows the XRD patterns of CuFe_2O_4 at different calcination temperatures. The diffraction peaks of CuFe_2O_4 –300 at $2\theta = 30.17^\circ, 35.54^\circ, 37.18^\circ, 43.20^\circ, 53.60^\circ, 57.14^\circ$ and 62.74° corresponding to the (220), (311), (222), (400), (422), (511) and (440) crystal faces of CuFe_2O_4 (#JCPDS77–0010), respectively. This indicates that the CuFe_2O_4 prepared by the sol–gel method has generated an obvious spinel structure, which is in agreement with the findings of Selima et al. [14]. According to Scherrer formula, when the calcination temperature is 300 °C, the lattice size on the (311) crystal plane is 18.2 nm [15]. There is a phase transformation from cubic CuFe_2O_4 (c- CuFe_2O_4) to tetragonal CuFe_2O_4 (t- CuFe_2O_4) at temperatures above 300 °C. The arrangement of crystal particles is more complete and denser. The CuFe_2O_4 –600 at $2\theta = 18.32^\circ, 34.72^\circ, 35.86^\circ, 41.82^\circ, 53.92^\circ, 62.16^\circ$ and 63.63° , corresponding to the tetragonal CuFe_2O_4 at (101), (103), (211), (004), (312), (224) and (400) crystal faces, which are in agreement with the standard card (#JCPDS34–0425). When the calcination temperature is 400–600 °C, there is the appearance of an impurity phase. The characteristic peak of CuO (#JCPDS48–1548) appears at 53.49° , indicating that there is a small amount of CuO. The characteristic peaks of α - Fe_2O_3 (JCPDS 84–0306) appear at $57.27^\circ, 62.92^\circ$ and 64.01° , confirming the presence of this phase. The XRD results show that the crystalline formation and particle size of the catalysts are affected by the calcination temperature.

Raman spectroscopy technique is one of the powerful techniques for a direct probe of cation redistribution, structural transformation, and lattice distortion. Figure 3 shows Raman spectra of CuFe_2O_4 calcined at 200, 300, 400, 500, and 600 °C. The structural transformation from cubic ($Fd\bar{3}m$) to tetragonal ($I4_1/amd$) symmetry occurs due to strengthening

of the Jahn–Teller distortion. In this study, five Raman characteristic peaks were observed for the CuFe_2O_4 calcined at 200 °C and 300 °C, which were present near 155 cm^{-1} ($T_{2g}(3)$), 280 cm^{-1} (E_g), 331 cm^{-1} ($T_{2g}(2)$), 470 cm^{-1} ($T_{2g}(1)$), 574 cm^{-1} ($A_{1g}(2)$) and 676 cm^{-1} ($A_{1g}(1)$). The Raman activity patterns present in the synthesized copper ferrate match well with the group theory results. These belong to cubic inverse–spinel copper ferrite. With the increase of calcination temperature, the copper ferrite samples gradually transformed into tetragonal phase structure, and new Raman spectral peaks appeared, such as 780 cm^{-1} , 840 cm^{-1} and 930 cm^{-1} . In the prepared CuFe_2O_4 , the presence of Raman modes the T_{2g} mode and the E_g mode in the lower frequency range demonstrates the stability of the spinel structure [16]. The peak at the $T_{2g}(1)$ mode is due to the asymmetric stretching of the oxygen anion with tetrahedral and octahedral cations. It can be observed that the vibrational frequency of the Raman–activated mode shifts to a lower frequency (red–shift) due to the redistribution of the cations and the relative increase of the particle size. The width of the Raman active modes is also increased. Due to the redistribution of cations between the tetrahedral and octahedral positions, the intensity of the peak the $A_{1g}(1)$ mode decreases with increasing calcination temperature, while the intensity of the remaining peaks increases [17].

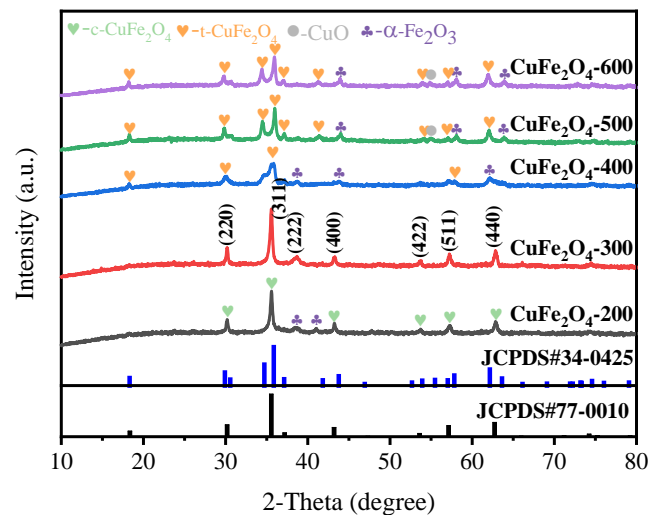


Figure 2. The XRD patterns of CuFe_2O_4 at different calcination temperatures.

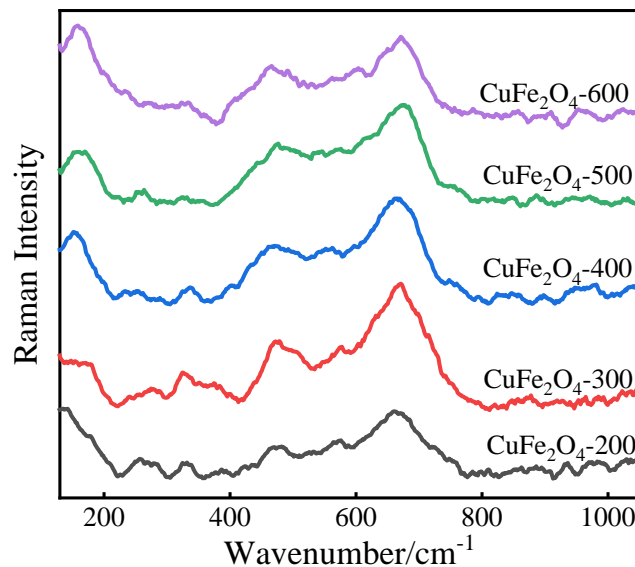


Figure 3. The Raman spectra of CuFe_2O_4 at different calcination temperatures.

Figure 4 shows the FT-IR spectra of CuFe_2O_4 calcined at $300\text{ }^\circ\text{C}$ before and after the degradation reaction. Spinel compounds are characterized by two lattice vibrations that correspond, respectively, to the vibrations of tetrahedral and octahedral metal centers against the O^{2-} cage. The first one appears in Figure 4 around 570 cm^{-1} while the other is not complete and is expected to be centered slightly below 400 cm^{-1} . [18]. These two bands confirm the formation of spinel structure and there is no significant change before and after the reaction. The absorption broadband at 3400 cm^{-1} indicates the stretching mode of the H_2O molecule $-\text{OH}$ group. The formation of the bands at 2925 cm^{-1} and 2960 cm^{-1} is due to the stretching vibrations of CH_2 and CH_3 . Moreover, bands due to $\text{C}=\text{O}$ stretching vibrations of the citric acid COOH group appear at 1635 cm^{-1} , indicating the binding of citric acid radicals to the magnetite surface. This band may also be the bending vibration of water [19]. The characteristic absorption band located near 1036 cm^{-1} is attributed to the $\text{C}-\text{O}-\text{C}$ stretching vibration. The CuFe_2O_4 also exhibits weak characteristic bands at 1380 cm^{-1} and 878 cm^{-1} , which represent the symmetric stretching vibration of the nitrate ion and the asymmetric stretching, etc. [20] From the FT-IR spectrum, it can be seen that citrate and nitrate impurities are very small. High-purity CuFe_2O_4 materials can be effectively prepared by the sol-gel method.

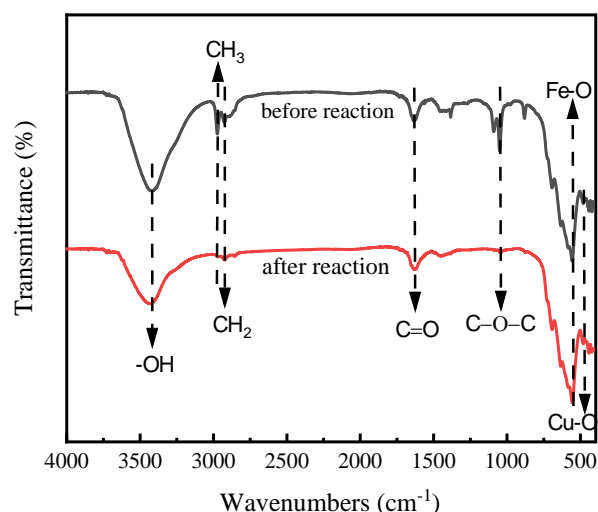


Figure 4. The FT-IR spectra of CuFe_2O_4 before and after degradation reaction.

3.2. TC Degradation Behavior

3.2.1. A Comparative Study of TC Removal in the Different System

As displayed in Figure 5a, the degradation efficiencies of different reaction systems were investigated. The degradation rate of TC was 0.3% when only PDS was added. This indicates that PDS could not produce free radicals rapidly in the absence of external catalysis [21]. When only CuFe_2O_4 was used (i.e., without PDS), the TC removal efficiency reached 34.0%, obviously as a result of adsorption but not degradation. In summary, the removal of TC by adsorption or single PDS degradation is relatively low. In the absence of PDS, the CuFe_2O_4 , UV and $\text{CuFe}_2\text{O}_4/\text{UV}$ were 34.0%, 7.8% and 50.6%, respectively. The highest degradation rate of TC reached 91.1% after adding PDS, which verified that PDS has a crucial role to play in the system, as the addition of PDS could generate more free radicals [22]. The UV lamp was the activator in the photocatalytic reaction. The degradation rate of TC was 61.5% in the case of activating PDS by UV radiation, which confirmed that PDS can be directly excited by UV light to make its $\text{O}-\text{O}$ bond break into $\text{SO}_4^{\bullet-}$ (Equation (1)). At the same time, UV radiation excites electrons from the valence band of CuFe_2O_4 into the conduction band. These electrons act as a strong reducing agent and result in the formation of $\text{SO}_4^{\bullet-}$ radicals as shown in Equation (2) [23]. The addition of CuFe_2O_4 was more effective compared to PDS activation by UV. The degradation of TC reached 91.1% in the $\text{CuFe}_2\text{O}_4/\text{UV}/\text{PDS}$ system, indicating the high catalytic efficiency

of CuFe_2O_4 in activating PDS. In addition, CuFe_2O_4 acts as a photocatalyst, where it can excite more different kinds of radicals in the system [24]. The above discussion shows that CuFe_2O_4 coupled with UV activated persulfate provides excellent degradation conditions for degrading TC. Firstly, both CuFe_2O_4 and UV can activate PDS. Secondly, the CuFe_2O_4 as a photocatalyst, it could excite more different kinds of radicals in the system.

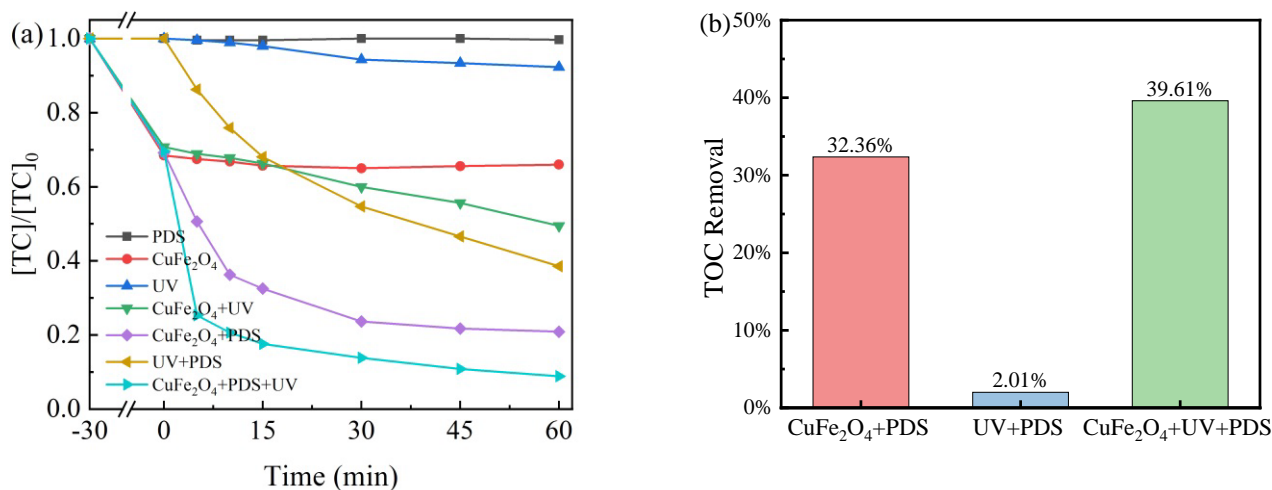
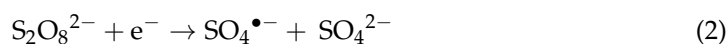


Figure 5. (a) TC degradation efficiency of the different systems investigated in this work (The CuFe_2O_4 was added 30 min before the reaction starts and that PDS is added at $t = 0$); (b) TOC of different systems. Experimental conditions: $[\text{TC}]_0 = 20 \text{ mg/L}$, $\text{pH} = 7$, $[\text{PDS}] = 0.7 \text{ mM}$, UV-light power = 30 W and CuFe_2O_4 dose = 0.2 g/L.

Meanwhile, the mineralization efficiency of TC at various catalytic conditions was evaluated by TOC measurement in the solution after 90 min of reaction. As shown in Figure 5b, the $\text{CuFe}_2\text{O}_4/\text{UV}/\text{PDS}$ system had the highest TOC removal rate which was 39.6%, followed by $\text{CuFe}_2\text{O}_4/\text{PDS}$. It indicates that the $\text{CuFe}_2\text{O}_4/\text{UV}/\text{PDS}$ system can achieve a high level of pollutant degradation.



In this work, the catalytic performance of calcination at different temperatures (200–600 °C) was compared, and the results are shown in Figure 6a. The degradation rates of TC were 87.4%, 91.1%, 86.2%, 85.7% and 82.6% at different calcination temperatures (200–600 °C), respectively. It shows that TC has high degradation efficiency at low calcination temperature, and the degradation rate of TC decreases with higher calcination temperature. Proper calcination can improve the catalytic performance of CuFe_2O_4 catalyst. As the calcination temperature increases, the crystal structure, specific surface area and oxygen vacancies of the catalyst will change, thereby affecting its catalytic performance. At an appropriate calcination temperature, the specific surface area and pore structure of the catalyst are optimized, and the catalytic activity and selectivity are improved. Excessive temperature can lead to an increase in particle size and lattice damage, thereby reducing catalytic activity [25]. In addition, as the calcination temperature increases, CuFe_2O_4 decomposes into separate oxides $\alpha\text{-Fe}_2\text{O}_3$ and CuO . To confirm that Fe_2O_3 and CuO affect the degradation rate of TC, a comparison test was also conducted in this section (Figure 6b), and under the same conditions, the removal rate by CuO as catalyst was 85.1% and that by Fe_2O_3 as a catalyst was 39.1%.

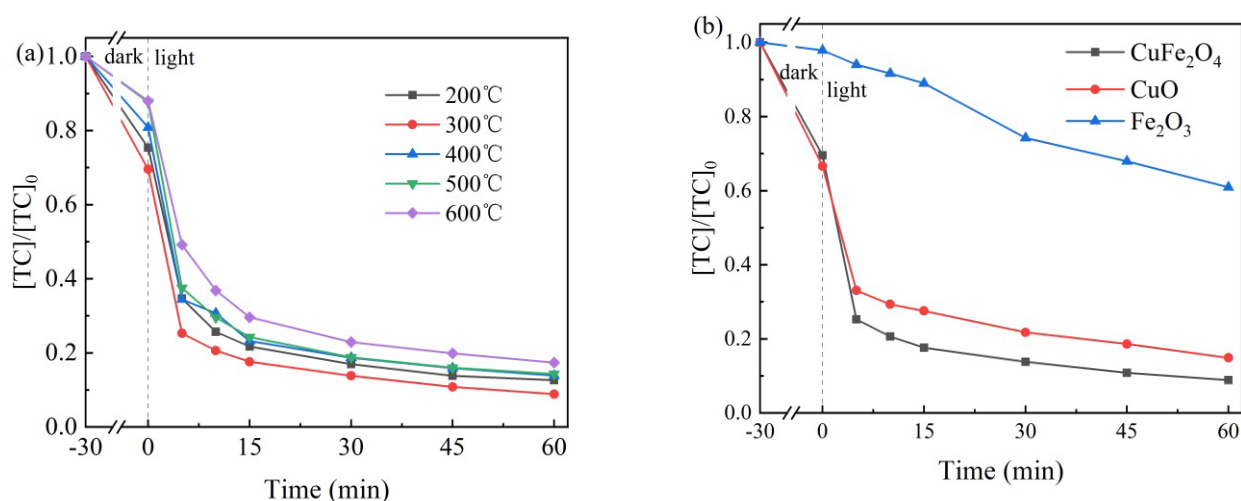


Figure 6. (a) Effect of different calcination temperatures of CuFe_2O_4 on TC degradation; (b) Effect of different catalysts on TC degradation. Experimental conditions: $[\text{TC}]_0 = 20 \text{ mg/L}$, $\text{pH} = 7$, $[\text{PDS}] = 0.7 \text{ mM}$, UV–light power = 30 W and CuFe_2O_4 dose = 0.2 g/L (CuO dose = 0.2 g/L and Fe_2O_3 dose = 0.2 g/L).

3.2.2. The Effect of Initial pH

Since the initial pH usually has an important influence on the generation process of free radicals, the physicochemical properties of the reactants and the oxidation capacity of the free radicals, the findings of the investigation of the initial solution pH are presented in Figure 7. Firstly, under alkaline conditions, the OH^- reacts with $\text{SO}_4^{\bullet-}$ to form $\bullet\text{OH}$, and the oxidation activity is weakened. The $\bullet\text{OH}$ reacts with $\bullet\text{OH}$ to form water and the free radicals are reduced, which leads to a decrease in the TC degradation rate (Equations (3)–(5)). The findings indicate that the TC removal is affected when the free radicals in the system are reduced [26]. Secondly, the TC degradation is also influenced by the charge of TC and the surface charge of CuFe_2O_4 [27,28]. The point of zero charge (pH_{zpc}) of CuFe_2O_4 was 5.95 (Figure 8a). The chemical structure of tetracycline was shown in Figure 8b. The hydroxyl groups are deprotonated at high pH, hence the negative charge, at low pH the amine groups are protonated and hence the positive charge. When $\text{pH} < 3$, the TC solution has a positive charge. When $\text{pH} = 3\text{--}7.7$, the TC in the solution exists as amphoteric ions. When $\text{pH} > 7.7$, it exists as monovalent anions or divalent anions. When $\text{pH} < \text{pH}_{\text{zpc}}$, the positive surface charge of the material will help to adsorb more $\text{SO}_4^{\bullet-}$ oxidized organic matter [29]. When $\text{pH} > \text{pH}_{\text{zpc}}$, the material surface is negatively charged and TC exists as monovalent anions, which generate an electrostatic repulsion between TC and the surface of CuFe_2O_4 . At $\text{pH} = 11$, there is no adsorption in the 30 min–period before the reaction. At $\text{pH} = 9$ and $\text{pH} = 3$, the amount adsorbed is much less than at $\text{pH} = 5$ and $\text{pH} = 7$. Under strong acid or alkali conditions, the surface of copper ferrite will suffer serious structural damage and loss of active site, leading to a significant reduction in its adsorption capacity. Under neutral condition, copper ferrite shows better adsorption performance, because its surface structure and active site can maintain good stability at this time. In addition, some experimental studies have also shown that copper ferrite under neutral conditions may undergo hydrogen bonding, van der Waals forces and charge transfer interactions with the adsorbent, thereby enhancing its adsorption capacity [30]. It prevents the reaction of TC on the material surface. Showing the high efficiency of $\text{CuFe}_2\text{O}_4/\text{UV}/\text{PDS}$ at neutral pH, the process is suitable for surface water and groundwater treatment.



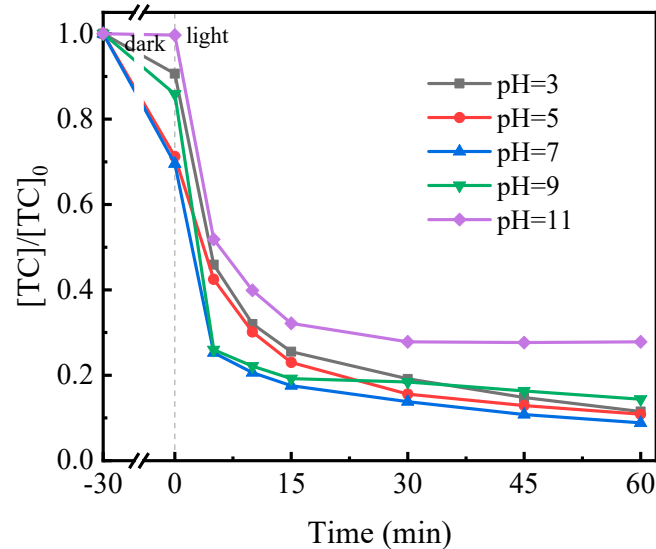


Figure 7. The effect of initial pH on TC degradation in CuFe₂O₄/UV/PDS system. Experimental conditions: [TC]₀ = 20 mg/L, [PDS] = 0.7 mM, UV–light power = 30 W and CuFe₂O₄ dose = 0.2 g/L.

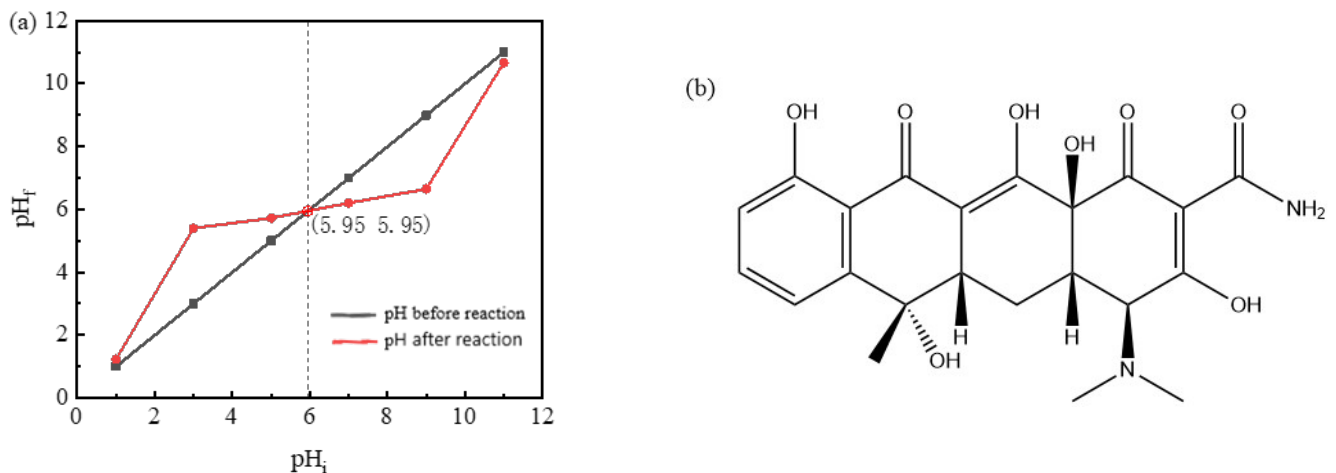


Figure 8. (a) The pH_{pazc} of CuFe₂O₄, (b) The chemical structure of tetracycline.

3.2.3. Stability and Recyclability of CuFe₂O₄

The stability and reusability of CuFe₂O₄ photocatalysts were confirmed through five consecutive reuse experiments. The CuFe₂O₄ is easily removed from the solution through magnetic means such as simple magnets [31]. It was separated from the system using a magnet after each degradation reaction and rinsed three times with deionized water. Then, put into a 60 °C oven to dry. Subsequently, the degradation experiment was performed again. As displayed in Figure 9, even after four cycles, the TC degradation rate remained above 84%. From the changes in TC adsorption, it is inferred that the minor decrease in the efficiency of removal may be attributed to limited poisoning of the catalyst surface by reaction intermediates and loss of CuFe₂O₄ particles during washing [32].

3.3. Degradation Reaction Mechanism

3.3.1. Identification of Active Species

To investigate the activation mechanism of the CuFe₂O₄/UV/PDS system, quenching experiments were performed. Based on the summary of previous studies [33–35], it

was concluded that $\text{SO}_4^{\bullet-}$ and $\bullet\text{OH}$ may be produced in the $\text{CuFe}_2\text{O}_4/\text{UV}/\text{PDS}$ system. Because of the different reaction rates of anhydrous ethanol (EtOH) and tert-butanol (TBA) with $\text{SO}_4^{\bullet-}$ and $\bullet\text{OH}$, the EtOH capture group and the TBA capture group were selected. The reaction rates of EtOH with $\text{SO}_4^{\bullet-}$ and $\bullet\text{OH}$ are $(1.6\text{--}7.7) \times 10^7 \text{ M}^{-1}\text{s}^{-1}$ and $(1.2\text{--}2.8) \times 10^9 \text{ M}^{-1}\text{s}^{-1}$ [36], respectively. As presented in Figure 10a, EtOH concentration and the degradation rate of TC were inversely related. When the EtOH concentration increased from 0 mM to 100 mM, the degradation rate of TC decreased by 32.2%. In addition, the reaction rate of TBA with $\bullet\text{OH}$ was higher than that of $\text{SO}_4^{\bullet-}$ ($k_{\bullet\text{OH}} = (3.8\text{--}7.6) \times 10^8 \text{ M}^{-1}\text{s}^{-1}$, $k_{\text{SO}_4^{\bullet-}} = (4.0\text{--}9.1) \times 10^5 \text{ M}^{-1}\text{s}^{-1}$) [37]. The removal rate of TC was 83.4% when the concentration of TBA was 100 mM (Figure 10b). Therefore, according to the difference between the degradation rate of TC under the participation of EtOH and TBA, it can be inferred that $\text{SO}_4^{\bullet-}$ plays a dominant role compared with $\bullet\text{OH}$. It is worth noting that the addition of ethanol and tert butanol does not completely stop the reaction, indicating that there may be other free radical or non-free radical pathways in the reaction system [38,39].

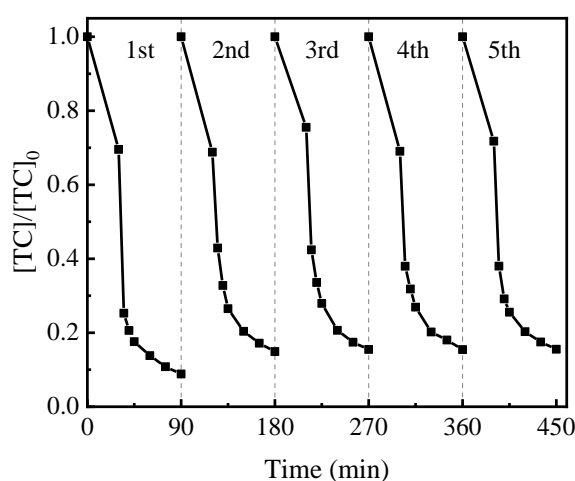


Figure 9. The stability and reusability of CuFe_2O_4 . Experimental conditions: $[\text{TC}]_0 = 20 \text{ mg/L}$, $\text{pH} = 7$, $[\text{PDS}] = 0.7 \text{ mM}$, UV-light power = 30 W and CuFe_2O_4 dose = 0.2 g/L.

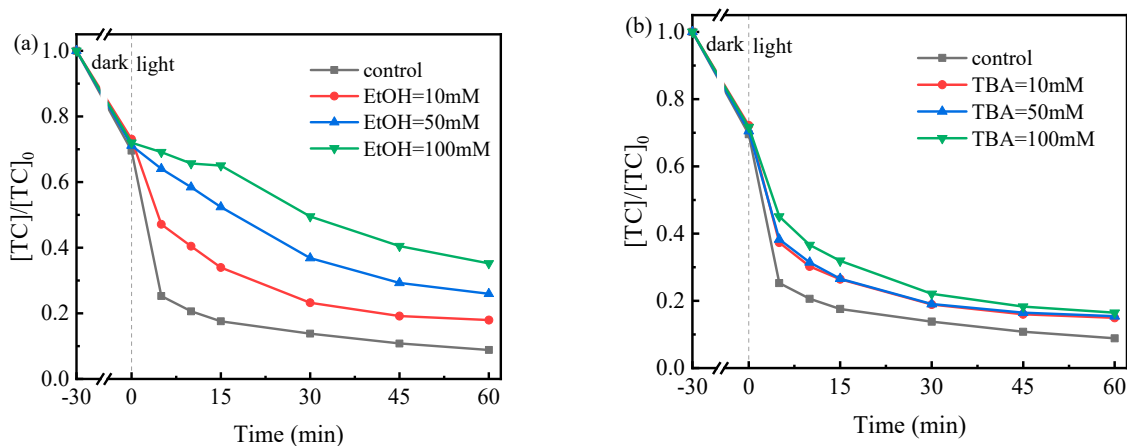


Figure 10. The effect of different (a) EtOH and (b) TBA, concentration on degradation of TC in $\text{CuFe}_2\text{O}_4/\text{UV}/\text{PDS}$ system. Experimental conditions: $[\text{TC}]_0 = 20 \text{ mg/L}$, $\text{pH} = 7$, $[\text{PDS}] = 0.7 \text{ mM}$, UV-light power = 30 W and CuFe_2O_4 dose = 0.2 g/L.

3.3.2. Mechanism of Degradation

According to the mentioned results and discussions, the possible mechanism for the TC degradation by $\text{CuFe}_2\text{O}_4/\text{UV}/\text{PDS}$ is proposed as shown in Figure 11. In the first step, the energy of some incident photons can destroy the chemical bond of TC molecule,

TC molecules will directly self-decompose. In addition, UV radiation can also directly activate PDS, generating sulfate radicals. Furthermore, the presence of photogenerated electrons on the surface of CuFe_2O_4 can activate PDS to generate $\text{SO}_4^{\bullet-}$. Secondly, the effective $\text{Fe}^{3+}/\text{Fe}^{2+}$ ($\text{Cu}^{2+}/\text{Cu}^{3+}$) conversion enhances the PDS activation and generates $\text{SO}_4^{\bullet-}$ and $\bullet\text{OH}$ for pollutant removal [40,41]. These produce free radicals react with TC, breaking it down into harmless H_2O , CO_2 and some intermediates.

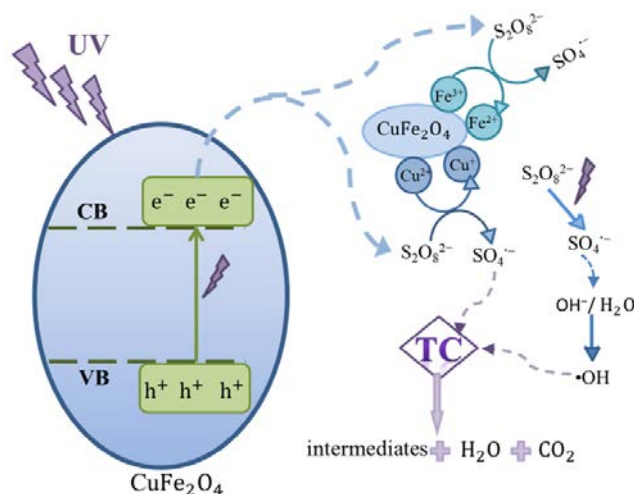


Figure 11. Schematic representation of the possible degradation mechanism of TC in the $\text{CuFe}_2\text{O}_4/\text{UV}/\text{PDS}$ system.

4. Conclusions

To summarize, the CuFe_2O_4 exhibits excellent performance in the degradation of tetracycline. In this process, several methods (XRD, Raman spectra spectroscopy, SEM and FT-IR) were carried out to characterize CuFe_2O_4 , demonstrating that magnetic separable CuFe_2O_4 nanoparticles can be prepared by the sol-gel method. Through the coupling of $\text{CuFe}_2\text{O}_4/\text{UV}/\text{PDS}$ process, the degradation rate of antibiotics was improved. It was confirmed that the coupling of the $\text{CuFe}_2\text{O}_4/\text{UV}$ has a synergistic effect on the catalytic PDS to produce more active species. Under optimal conditions, the TC degradation rate reached 91.1% within 90 min. Magnetic CuFe_2O_4 powder can be effectively recycled, and reusability and stability experiments confirmed the excellent stability and cyclicality of the CuFe_2O_4 catalyst. In addition, through quenching experiments, it was concluded that there is $\text{SO}_4^{\bullet-}$ and $\bullet\text{OH}$ generation in the system. A possible mechanism of degradation was proposed. It confirmed its potential application in degrading antibiotics.

Author Contributions: Conceptualization, B.L. and Y.C.; Data curation, P.M., Y.S. and J.Z.; Formal analysis, P.M. and Y.S.; Funding acquisition, B.L.; Methodology, J.Z. and W.Z.; Supervision, Y.C. and B.L.; Writing—original draft, Y.S.; Writing—review & editing, P.M. and B.L. All authors have read and agreed to the published version of the manuscript.

Funding: This research was funded by Key Research and Extension Project of Henan Province (222102320291).

Institutional Review Board Statement: Not applicable.

Informed Consent Statement: Not applicable.

Data Availability Statement: All data used to support the findings of this study are included within the article.

Conflicts of Interest: The authors declare that they have no conflict of interest regarding the publication of this paper.

References

1. Zhang, Y.; Maqbool, F.; Hu, Y. Removal of antibiotics pollutants in wastewater by UV-based advanced oxidation processes: Influence of water matrix components, processes optimization and application: A Review. *J. Water Process Eng.* **2022**, *45*, 102496. [[CrossRef](#)]
2. Abd, E.M.; Eltaweil, A.S.; Elshishini, H.M. Sustainable adsorptive removal of antibiotic residues by chitosan composites: An insight into current developments and future recommendations. *Arab. J. Chem.* **2022**, *15*, 103743. [[CrossRef](#)]
3. Qi, N.; Wang, P.; Wang, C.; Ao, Y. Effect of a typical antibiotic (tetracycline) on the aggregation of TiO₂ nanoparticles in an aquatic environment. *J. Hazard. Mater.* **2018**, *341*, 187–197. [[CrossRef](#)]
4. Chen, G.; Yu, Y.; Liang, L. Remediation of antibiotic wastewater by coupled photocatalytic and persulfate oxidation system: A critical review. *J. Hazard. Mater.* **2021**, *408*, 124461. [[CrossRef](#)]
5. Cai, J.; Xie, J.; Xing, L. Enhanced mechanism of carbamazepine degradation by electrochemical activation of persulfate in flow-through system. *Sep. Purif. Technol.* **2022**, *301*, 122021. [[CrossRef](#)]
6. Zrinyi, N.; Pham, A.L. Oxidation of benzoic acid by heat-activated persulfate: Effect of temperature on transformation pathway and product distribution. *Water Res.* **2017**, *120*, 43–51. [[CrossRef](#)]
7. Chen, W.; Su, Y. Removal of dinitrotoluenes in wastewater by sono-activated persulfate. *Ultrason. Sonochem.* **2012**, *19*, 921–927. [[CrossRef](#)]
8. Zhou, Y.; Xiang, Y.; He, Y.; Yang, Y.; Zhang, J.; Luo, L.; Peng, H.; Dai, C.; Zhu, F.; Tang, L. Applications and factors influencing of the persulfate-based advanced oxidation processes for the remediation of groundwater and soil contaminated with organic compounds. *J. Hazard. Mater.* **2018**, *359*, 396–407. [[CrossRef](#)]
9. Li, Z.; Guo, C.; Lu, J.; Hu, Z.; Ge, M. Tetracycline degradation by persulfate activated with magnetic Cu/CuFe₂O₄ composite: Efficiency, stability, mechanism and degradation pathway. *J. Hazard. Mater.* **2019**, *373*, 85–96. [[CrossRef](#)]
10. Xu, Y.; Ai, J.; Zhang, H. The mechanism of degradation of bisphenol A using the magnetically separable CuFe₂O₄/peroxymonosulfate heterogeneous oxidation process. *J. Hazard. Mater.* **2016**, *309*, 87–96. [[CrossRef](#)]
11. Jing, P.; Li, J.; Pan, L.; Wang, J.; Sun, X.; Liu, Q. Efficient photocatalytic degradation of acid fuchsin in aqueous solution using separate porous tetragonal-CuFe₂O₄ nanotubes. *J. Hazard. Mater.* **2015**, *284*, 163–170. [[CrossRef](#)]
12. Yang, M.; Ren, X.; Hu, L.; Guo, W.; Zhan, J. Facet-controlled activation of persulfate by goethite for tetracycline degradation in aqueous solution. *Chem. Eng. J.* **2021**, *412*, 128628. [[CrossRef](#)]
13. Zhao, Y.; Lin, C.; Bi, H.; Liu, Y.; Yan, Q. Magnetically separable CuFe₂O₄/AGBR composite photocatalysts: Preparation, characterization, photocatalytic activity and photocatalytic mechanism under Visible light. *Appl. Surf. Sci.* **2017**, *392*, 701–707. [[CrossRef](#)]
14. Selima, S.S.; Khairy, M.; Mousa, M.A. Comparative studies on the impact of synthesis methods on structural, optical, magnetic and catalytic properties of CuFe₂O₄. *Ceram. Int.* **2019**, *45*, 6535–6540. [[CrossRef](#)]
15. Chang, S.; Mei, S.; Qianqian, R.; Yang, L.; Yang, L.; Lu, Z.; Shuang, W.; Wen, G. Effect of synthesis conditions on the structure and properties of LiFeO₂/ZnFe₂O₄ nanocomposites prepared by a sol-gel method. *Solid State Commun.* **2021**, *334*, 114379. [[CrossRef](#)]
16. Xu, Y.; Sherwood, J.; Qin, Y.; Holler, R.A.; Bao, Y. A general approach to the synthesis and detailed characterization of magnetic ferrite nanocubes. *Nanoscale* **2015**, *7*, 12641–12649. [[CrossRef](#)]
17. Chatterjee, B.K.; Bhattacharjee, K.; Dey, A.; Ghosh, C.K.; Chattopadhyay, K.K. Influence of spherical assembly of copper ferrite nanoparticles on magnetic properties: Orientation of Magnetic Easy Axis. *Dalton Trans.* **2014**, *43*, 7930–7944. [[CrossRef](#)]
18. Verma, K.; Kumar, A.; Varshney, D. Effect of Zn and Mg doping on structural, dielectric and magnetic properties of tetragonal CuFe₂O₄. *Curr. Appl. Phys.* **2013**, *13*, 467–473. [[CrossRef](#)]
19. Soufi, A.; Hajjaoui, H.; Elmoubarki, R. Heterogeneous Fenton-like degradation of tartrazine using CuFe₂O₄ nanoparticles synthesized by sol-gel combustion. *Appl. Surf. Sci. Adv.* **2022**, *9*, 100251. [[CrossRef](#)]
20. Wang, L.; Ma, X.; Huang, G. Construction of ternary CuO/CuFe₂O₄/g-C₃N₄ composite and its enhanced photocatalytic degradation of tetracycline hydrochloride with persulfate under simulated sunlight. *J. Environ. Sci.* **2022**, *112*, 59–70. [[CrossRef](#)]
21. Dong, W.; Cai, T.; Liu, Y.; Wang, L.; Chen, H.; Zeng, W.; Li, J.; Li, W. Rapid removal of organic pollutants by a novel persulfate/brochantite system: Mechanism and implication. *J. Colloid Interface Sci.* **2021**, *585*, 400–407. [[CrossRef](#)]
22. Lee, J.; von Gunten, U.; Kim, J.H. Persulfate-based advanced oxidation: Critical assessment of opportunities and roadblocks. *Environ. Sci. Technol.* **2020**, *54*, 3064–3081. [[CrossRef](#)]
23. Ma, Q.; Nengzi, L.; Zhang, X. Enhanced activation of persulfate by AC@CoFe₂O₄ nanocomposites for effective removal of lomefloxacin. *Sep. Purif. Technol.* **2020**, *233*, 115978. [[CrossRef](#)]
24. Yin, R.; Chen, Y.; Hu, J.; Lu, G.; Zeng, L.; Choi, W.; Zhu, M. Complexes of Fe(III)-organic pollutants that directly activate Fenton-like processes under Visible light. *Appl. Catal. B-Environ.* **2021**, *283*, 119663. [[CrossRef](#)]
25. María, V.; López, R.; Miguel, A. Effect of calcination temperature of a copper ferrite synthesized by a sol-gel method on its structural characteristics and performance as Fenton catalyst to remove gallic acid from water. *J. Colloid Interface Sci.* **2018**, *511*, 193–202. [[CrossRef](#)]
26. Rajabi, S.; Nasiri, A.; Hashemi, M. Enhanced activation of persulfate by CuCoFe₂O₄@MC/AC as a novel nanomagnetic heterogeneous catalyst with ultrasonic for metronidazole degradation. *Chemosphere* **2022**, *286*, 131872. [[CrossRef](#)]
27. Qiao, L.; Shi, Y.; Cheng, Q.; Liu, B.; Liu, J. The removal efficiencies and mechanism of aniline degradation by peroxydisulfate activated with magnetic Fe-Mn oxides composite. *J. Water Reuse Desalination* **2021**, *11*, 212–223. [[CrossRef](#)]

28. Ramu, A.; Salla, S.; Gopi, S.; Silambarasan, P.; Yang, D.; Song, M.; Ali, H.; Salem, M.; Choi, D. Surface-tuned hierarchical γ -Fe₂O₃-N-RGO nanohydrogel for efficient catalytic removal and electrochemical sensing of toxic nitro compounds. *Chemosphere* **2021**, *268*, 128853. [[CrossRef](#)]
29. Tan, C.; Gao, N.; Fu, D. Efficient degradation of paracetamol with nanoscaled magnetic CoFe₂O₄ and MnFe₂O₄ as a heterogeneous catalyst of peroxymonosulfate. *Sep. Purif. Technol.* **2017**, *175*, 47–57. [[CrossRef](#)]
30. Shi, Y.; Ma, P.; Qiao, L.; Liu, B. Fe–Mn Oxide Composite Activated Peroxydisulfate Processes for Degradation of p–Chloroaniline: The Effectiveness and the Mechanism. *Processes* **2022**, *10*, 2227. [[CrossRef](#)]
31. Belessiotis, G.V.; Falara, P.P.; Ibrahim, I.; Kontos, A.G. Magnetic Metal Oxide–Based Photocatalysts with Integrated Silver for Water Treatment. *Materials* **2022**, *15*, 4629. [[CrossRef](#)] [[PubMed](#)]
32. Zheng, X.; Chu, Y.; Miao, B.; Fan, J. Ag-doped Bi₂WO₆/BiOI heterojunction used as photocatalyst for the enhanced degradation of tetracycline under visible-light and biodegradability improvement. *J. Alloys Compd.* **2022**, *893*, 162382. [[CrossRef](#)]
33. Liu, Y.; Guo, H.; Zhang, Y. Heterogeneous activation of persulfate for Rhodamine B degradation with 3D flower sphere-like BiOI/Fe₃O₄ microspheres under visible light irradiation. *Sep. Purif. Technol.* **2018**, *192*, 88–98. [[CrossRef](#)]
34. Pan, J.; Guo, F.; Sun, H.; Li, M.; Zhu, X.; Gao, L.; Shi, W. CdS nanoparticles decorated hexagonal Fe₂O₃ nanosheets with a Z-scheme photogenerated electron transfer path for improved visible-light photocatalytic hydrogen production. *Chin. J. Chem. Eng.* **2021**, *56*, 6663–6675. [[CrossRef](#)]
35. Sun, H.; Guo, F.; Pan, J.; Huang, W.; Wang, K.; Shi, W. One-pot thermal polymerization route to prepare N-deficient modified G–C₃N₄ for the degradation of tetracycline by the synergistic effect of photocatalysis and persulfate-based advanced oxidation process. *Chem. Eng. J.* **2021**, *406*, 126844. [[CrossRef](#)]
36. Zhang, H.; Song, Y.; Nengzi, L. Activation of persulfate by a novel magnetic CuFe₂O₄/Bi₂O₃ composite for lomefloxacin degradation. *Chem. Eng. J.* **2020**, *379*, 122362. [[CrossRef](#)]
37. Sarkar, P.; Roy, D.; Bera, B. Efficient photocatalytic degradation of ciprofloxacin using novel dual Z-scheme gCN/CuFe₂O₄/MoS₂ mediated peroxymonosulphate activation. *Chem. Eng. J.* **2022**, *430*, 132834. [[CrossRef](#)]
38. Elashery, S.E.A.; Ibrahim, I.; Gomaa, H.; El-Bouraie, M.M.; Moneam, I.A.; Fekry, S.S.; Mohamed, G.G. Comparative Study of the Photocatalytic Degradation of Crystal Violet Using Ferromagnetic Magnesium Oxide Nanoparticles and MgO–Bentonite Nanocomposite. *Magnetochemistry* **2023**, *9*, 56. [[CrossRef](#)]
39. Ibrahim, I.; Belessiotis, G.V.; Antoniadou, M.; Kaltzoglou, A. Silver decorated TiO₂/g–C₃N₄ bifunctional nanocomposites for photocatalytic elimination of water pollutants under UV and artificial solar light. *Results Eng.* **2022**, *14*, 100470. [[CrossRef](#)]
40. Huang, X.; Zhu, N.; Wei, X.; Ding, Y.; Ke, Y.; Wu, P.; Liu, Z. Mechanism insight into efficient peroxydisulfate activation by novel Nano Zero-valent iron anchored γ Co₃O₄ (nzvi/ γ Co₃O₄) composites. *J. Hazard. Mater.* **2020**, *400*, 123157. [[CrossRef](#)]
41. Dang, V.C.; Tran, D.T.; Phan, A.T.; Pham, N.K.; Nguyen, V.N. Synergistic effect for the degradation of tetracycline by rGO–Co₃O₄ assisted Persulfate Activation. *J. Phys. Chem. Solids* **2021**, *153*, 110005. [[CrossRef](#)]

Disclaimer/Publisher’s Note: The statements, opinions and data contained in all publications are solely those of the individual author(s) and contributor(s) and not of MDPI and/or the editor(s). MDPI and/or the editor(s) disclaim responsibility for any injury to people or property resulting from any ideas, methods, instructions or products referred to in the content.